CORA Cork Open Research Archive
Cartlann Taighde Oscailte Chorcaí

Title	Pattern formation induced by an electric field in a polymer-air-polymer thin film system
Authors	Amarandei, George;Beltrame, Philippe;Clancy, Ian;O'Dwyer, Colm;Arshak, Arousian;Steiner, Ullrich;Corcoran, David;Thiele, Uwe
Publication date	2012-05-10
Original Citation	Amarandei, G., Beltrame, P., Clancy, I., O'Dwyer, C., Arshak, A., Steiner, U., Corcoran, D. and Thiele, U. (2012) 'Pattern formation induced by an electric field in a polymer-air-polymer thin film system', Soft Matter, 8(23), pp. 6333-6349. doi: 10.1039/C2SM25273B
Type of publication	Article (peer-reviewed)
Link to publisher's version	http://pubs.rsc.org/en/content/articlepdf/2012/sm/c2sm25273b - 10.1039/C2SM25273B
Rights	© Royal Society of Chemistry 2018
Download date	2026-11-10 22:12:34
Item downloaded from	https://hdl.handle.net/10468/6199

UCC
University College Cork, Ireland
Coláiste na hOllscoile Corcaigh

Pattern formation induced by an electric field in a polymer-air-polymer thin film system†

George Amarandei,[a*] Philippe Beltrame,[b] Ian Clancy,[a] Colm O'Dwyer,[a] Arousian Arshak,[a] Ullrich Steiner,[c] David Corcoran,[a] and Uwe Thiele[d]

Received Xth XXXXXXXXXX 20XX, Accepted Xth XXXXXXXXX 20XX
First published on the web Xth XXXXXXXXXX 200X
DOI: 10.1039/b000000x

Strong electric fields produce forces that can overcome the surface tension in thin liquid polymer films and in this way induce an instability of the free surface of the film, that triggers the formation of structures on a micrometer length scale. Here, we study experimentally a polymer-air-polymer system for several combinations of polymer films. These results are accompanied by theoretical considerations based on coupled long-wave time evolution equations for the two free surface profiles. The linear stability and nonlinear time evolution are investigated and compared to the experimental findings. The prediction that the instability always evolves through a mirror mode that couples the two surfaces in an anti-phase manner agrees well with the experimental results. The model describes well the linear (early stage) evolution of the instability. In the non-linear (later stage) evolution, topographical differences in the instability pattern occur if the mobilities of the two layers significantly differ and an unpredicted acceleration of growth is seen in thinner less mobile films. Possible reasons for the mismatch are discussed.

1 Introduction

The understanding and control of the dynamics of structuring processes of thin liquid films is a challenge in nanotechnological applications. In the absence of further influences, surface tension damps the capillary waves on the free surface of such films that are excited by thermal noise. However, the film surface and therefore an initially flat film may be destabilized by the presence of additional forces such as van der Waals forces for films of partially wetting or nonwetting apolar liquids[1,2], Marangoni forces due to heating from below[3,4] or an electric pressure exerted on a dielectric liquid in a capacitor[5–7]. When such a destabilizing force is present a band of wavenumbers in the capillary wave spectrum may be destabilized and a fastest growing mode will be selected[8,9]. The existence of the instability of the free surface of the film, its fastest growing wavelength and corresponding growth rate can be predicted by a linear stability analysis, e.g., of a long-wave hydrodynamic model[10,11]. In general, the dispersion relation $\beta(k)$, i.e. the dependence of the growth rate β on the wavenumber k determines the temporal evolution of all modes, with positive (negative) values of β corresponding to an amplification (damping) of the mode[10,12,13]. This approach is used to predict the typical structure length evolving in the instability of a polymer-air interface when van der Waals forces[2,14–16] and/or an electric field gradient are present[6,17–21].

When the surface of a thin polymer film is destabilized through the action of external electric field gradients, a process of self-organisation and pattern formation is triggered[5,6,17–20]. In a typical experimental setup in a one layer geometry (see Fig. 1a), a thin glassy polymer film is placed in a capacitor and subsequently brought above its glass transition temperature. Then the high electric fields generate interfacial pressures that are strong enough to destabilize the film of liquid polymer by overcoming surface tension. The amplitude of the selected linear mode grows first exponentially, then nonlinear effects set in and the growth continues until the maxima of film elevations touch the other conducting substrate. In this way an array of liquid columns is formed that connect the two substrates. The nonlinear growth process and potentially also the electrostatic repulsion between the columns may lead to their arrangement in lattices with different symmetries (square, hexagonal). Their geometry, however,

† Electronic Supplementary Information (ESI) available: [details of any supplementary information available should be included here]. See DOI: 10.1039/b000000x/

[a] *Department of Physics & Energy, University of Limerick, Ireland. Fax: +353 61 202423; Tel: +353 61 202625; E-mail: george.amarandei@ul.ie*
[b] *Dept. de Physique, UMR 1114 EmmaH, Université d'Avignon, F-84000 Avignon, France*
[c] *Department of Physics, University of Cambridge, Cavendish Laboratory, JJ Thomson Avenue, Cambridge, CB3 0HE, UK*
[d] *Department of Mathematical Sciences, Loughborough University, Loughborough, Leicestershire, LE11 3TU, UK*

does not always remain the same over the entire area of the probe, a coexistence of different patterns is sometimes observed [6,17,18]. The packing order of the columns is controlled by the film thickness, and an almost perfect hexagonal distribution is observed for a specific ratio of the film thickness with respect to the air gap [17,22].

We have explained that the destabilization of a simple polymer-air interface by an electric field (Fig. 1a) leads to pattern formation. However, if one replaces the air layer by a second liquid, as in the example of the polymer-polymer system sketched in Fig. 1b, one observes a reduction of the length scale of the instability induced by the electric field due to a reduction in the interfacial tension [7,21,23–25]. The dynamics change as well, as the mobilities of the two layers interact in the evolution of the instability [21]. If one adds a third layer to the set-up, by introducing an air layer above the polymer-polymer bilayer (see Fig. 1c) [26–30], the behaviour of the system becomes richer. For certain parameter values it allows for a sequential growth of the electrohydrodynamic instabilities of the two interfaces leading to the formation of patterns with two independent length scales. The primary structure size is about 10 times larger than the widths of the structures formed by the secondary instability [31]. Theoretical investigations for the type of two-layer systems sketched in Fig. 1c exist for the case of dewetting without electrical fields [26–28,32], and for the case of a destabilizing electric field [33].

The present paper describes an experimental and theoretical investigation into the destabilization and structuring process of the interfaces in a new configuration with two liquid layers and two free liquid-gas interfaces. We consider the polymer-air-polymer system sketched in Fig. 1d where two polymer films of thickness h_1 and h_2 are situated on two opposite solid substrates and are separated by an air layer. The two substrates are situated at a distance d and a potential U is applied between them. Recently, Srivastava et al.[34] presented a theoretical investigation of this geometry showing that it may be used to obtain ordered microstructures, i.e., it can be used to create periodic patterns on a large surface area. Their numerical simulations reveal that independently of the starting configuration mode, i.e. either in-phase bending (here, called a "zig-zag" mode) or anti-phase squeezing (here, referred to as a "mirror mode", sometimes also called a "varicose mode" [27]), the interfaces will always deform in an "antiphase squeezing mode". They showed that, although, a change in transport coefficients may occur as the viscosities alter the pathway of evolution, the final topography of the surfaces is controlled by the equilibrium thermodynamics of the system, i.e., by the underlying energy functional [32]. Thus, when there are large differences in viscosity between the two films, in the initial stages of evolution, the height of the features differ. Towards the final stages, the heights characterising the surface topographies become similar. For different surface energies, the final topographies revealed taller (shorter) columns in the films with less (more) surface energy. Based, on their 3D simulations they observed that for identical films the growing columns meet exactly at the middle of the air gap [34]. No experimental investigation of the polymer-air-polymer system has been presented to date.

In the present study we experimentally investigate such a polymer-air-polymer system for different film thicknesses, permittivities, viscosities and separations between the layers, and analyse characteristics including the typical instability wavelength and evolving surface topography. A theoretical model is proposed to explain the experimental findings. In contrast to the results obtained for the polymer-polymer-air system [26–30] it is not possible to induce different instabilities in the two respective films by the electric field as in the present experimental conditions the two polymer layers are not mechanically connected. Instead, it is analytically predicted that a coupled mode will dominate, leading to mirrored features, which is in good agreement with the experimental results presented here. Our prediction for the wavelength of the instability is also shown to be in good agreement with experimental observations. The topography of the two layers is experimentally seen to differ depending on the mechanical properties (viscosity or film thickness ratio) of the two layers. Although the model predicts well the linear and nonlinear behaviour for some of the experimental parameters, it is less successful in other cases. In particular, the nonlinear stage in the case of a large contrast in the mobilities of the two layers results in differences between the topographies of the model predictions and the experimental observations. In the late stage, the growth of the air-polymer interface structures on the less mobile thinner of the two films becomes faster than theoretically predicted. We argue that this effect may be linked to the dependence of polymer film viscosity on film thickness.

The paper is structured as follows. Section 2 describes our experimental methods, whereas section 3 introduces the long-wave model for the polymer-air-polymer system and its linear analysis. Subsequently, section 4 presents and relates theoretical and experimental results focusing on various practically important aspects of the evolution of the instability triggered by the electric field such as the wavelength and growth of the evolving surface modulations, the mirroring of surface structures of the two liquid air interfaces, and the resulting topography of the thin films. The different behaviour of the system that is

 This journal is © The Royal Society of Chemistry [year]

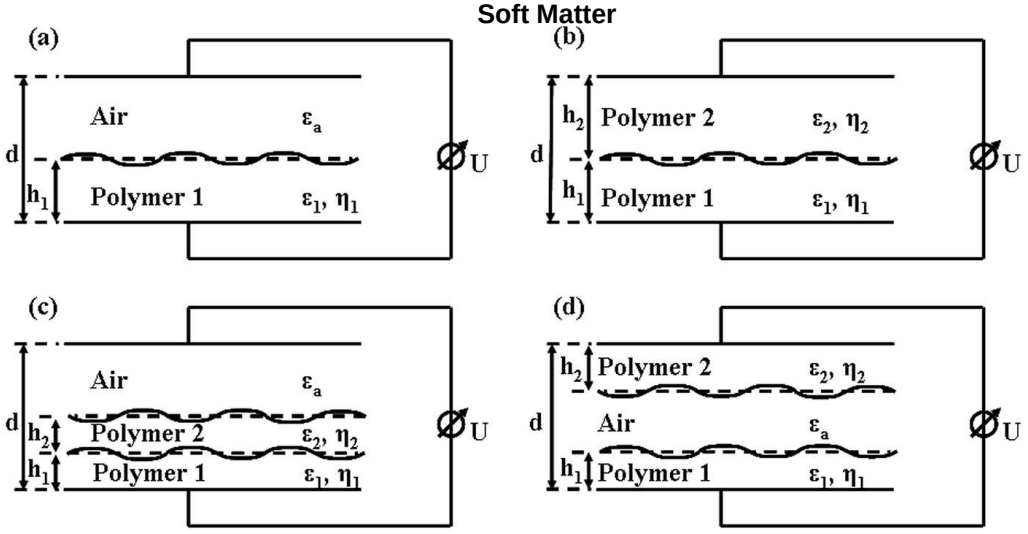


Fig. 1 Sketch of typical two-dimensional configurations for experiments with polymer layers in capacitors: (a) polymer-air system[6,17–20], (b) polymer-polymer system[7,21,23–25], (c) polymer-polymer-air system[26–30], and (d) the polymer-air-polymer geometry used here where the two polymer layers are energetically but not mechanically coupled. The local thicknesses of the layers are h_j with $j = 1, 2$; d is the separation between the capacitor plates, ϵ_j, and η_j are the dielectric constants and the viscosities of the two polymers respectively.

observed depending on the various control parameters is discussed and explained throughout section 4. Section 5 presents conclusions, provides comparisons with the literature and gives an outlook on future research.

2 Materials and methods

The polymers used in the experiments were polystyrene (PS) with an average molecular weight of $M_w = 10, 30, 100$, and $150\,\mathrm{kg\,mol^{-1}}$ with polydispersity index PDI $\leq$ 1.04 and poly(methyl methacrylate) (PMMA) with $M_w = 10$, and $100\,\mathrm{kg\,mol^{-1}}$ with PDI ≤ 1.05 purchased from Sigma-Aldrich. For simplicity we use abbreviations that include the molecular weight. For example, polystyrene with $M_w = 10\,\mathrm{kg\,mol^{-1}}$ is denoted "PS 10".

Si wafers with a resistivity of $2 - 3\,\Omega\,\mathrm{cm^{-1}}$ were cleaned in a jet of CO_2 ice crystals, and used as substrates on which thin polymer films of different thicknesses were spin coated from a solution of 2-3% polymer in toluene. For good electrical contact 5 nm Cr and 40 nm Au films were deposited on the backside of the wafers prior to spin coating. The experiments were performed in a convection oven at 170 °C using the polymer-air-polymer configuration as shown in Fig. 1d with Si microspheres of 1 μm diameter acting as spacers. A voltage $U = 50$ V dc was used to perturb the air/polymer interfaces. The films were used as cast and they were not annealed prior to destabilisation. During the experiments the current through the capacitor was monitored. After a transient period during initial heating, a small constant current was observed ($1 - 60$ mA). If significantly large changes in the current or short-circuits occurred, the sample was disregarded.

After time periods varying from 15 minutes to hours the perturbed thin polymer films were immobilized by quenching them to room temperature in the presence of the electric field. The two electrodes were mechanically separated and their surface topography was investigated by optical microscopy and atomic force microscopy (AFM). The AFM images were obtained employing non-contact or tapping mode. To characterize the surface topography the roughness (root mean square average of height deviations) was calculated using

$$R = \sqrt{\frac{\sum_i (\delta h_i)^2}{N}}, \qquad (1)$$

where δh_i is the local deviation of film height from the average value and N is the number of points where the height is measured (see the caption of Fig. 12). The wavelength of the evolving surface instability was calculated using a Fourier transform and it was found to be constant within the experimental error (≈10%) across the films. The viscosity ratios are calculated using the bulk viscosities that are obtained for each polymer using the WLF model[35] and the constants c_1 and c_2[36,37].

3 Theory

3.1 Modelling

To describe the polymer-air-polymer system sketched in Fig. 1d, equations that describe the profile evolution of the two liquid-air interfaces are derived from the Navier-Stokes equations following standard long-wave methods[10–12] as previously applied to liquid-liquid-gas layers[11,26–28,32].

For sufficiently viscous and thin liquid layers, the dynamics are slow and inertia is negligible as compared to viscous stress, i.e., the thin film dynamics corresponds to a small-Reynolds number flow. The viscous stress is high due to the large viscosity of the polymers and the hydrodynamic no-slip condition that is used at the substrate. The resulting creeping flow corresponds to a quasistatic balance between viscous and external forces. Assuming the ratio of vertical to horizontal length scales to be small, one may apply a long-wave approximation, and derive coupled thin film evolution (or lubrication) equations that govern the dynamics of the two liquid layers. In general, two polymer layers might be coupled mechanically and energetically. Both couplings act if the two layers are in direct mechanical contact as is the case in the liquid-liquid-air geometry (Fig. 1c)[27]. Here, however, the two polymer layers of the polymer-air-polymer system are separated by an air gap, i.e. they are not in direct mechanical contact and the coupling between them is purely energetic. For the experimental parameters used here, the energetic coupling only results from the electric field contribution f_{el} to the local free energy of the system, i.e. deformations of one layer change the electrical field in the gap that in turn influences the other layer. Van der Waals interactions are neglected as their contribution to the energy is very small for the layer thicknesses employed[6,17]. For isothermal films, the evolution equations for the two film thicknesses, $h_1(x,y,t)$ and $h_2(x,y,t)$, are given by

$$\partial_t h_j = -\nabla\cdot\left[\frac{h_j^3}{3\eta_j}\nabla\left(\sigma_j\Delta h_j - \partial_{h_j} f_{el}\right)\right]. \qquad (2)$$

where $j=1,2$, and η_j and σ_j are the bulk viscosity and the surface tension of polymer layer j respectively. The energy f_{el} will be discussed below. To bring the system into a non-dimensional form one introduces non-dimensional variables (with tildes)

$$h_j = d\widetilde{h}_j, \qquad x = d\sqrt{\frac{d}{\lambda_{el}}}\widetilde{x}, \qquad t=\tau\widetilde{t},$$
$$f_{el} = \kappa_{el}\widetilde{f}_{el}, \qquad \epsilon_j = \epsilon_a\widetilde{\epsilon}_j,$$

with the scales

$$\kappa_{el} = \epsilon_0\epsilon_a\frac{U^2}{d}, \quad \lambda_{el} = \epsilon_0\epsilon_a\frac{U^2}{\sigma_1}, \quad \tau = \frac{3\eta_1}{\lambda_{el}^2\sigma_1}d^3. \qquad (3)$$

The resulting non-dimensional time evolution equations are

$$\partial_{\widetilde{t}}\widetilde{h}_1 = -\widetilde{\nabla}\cdot\left[\widetilde{h}_1^3\widetilde{\nabla}\left(\tilde{\Delta}\widetilde{h}_1 - \partial_{\widetilde{h}_1}\widetilde{f}_{el}\right)\right] \qquad (4a)$$

$$\partial_{\widetilde{t}}\widetilde{h}_2 = -\widetilde{\nabla}\cdot\left[\frac{\widetilde{h}_2^3}{\eta}\widetilde{\nabla}\left(\sigma\tilde{\Delta}\widetilde{h}_2 - \partial_{\widetilde{h}_2}\widetilde{f}_{el}\right)\right] \qquad (4b)$$

where the non-dimensional energy $\widetilde{f}_{el}$ is

$$\widetilde{f}_{el}(\widetilde{h}_1,\widetilde{h}_2) = -\left[1+\widetilde{h}_1\left(\frac{1}{\widetilde{\epsilon}_1}-1\right)+\widetilde{h}_2\left(\frac{1}{\widetilde{\epsilon}_2}-1\right)\right]^{-1}.$$

Here $\widetilde{\epsilon_j}$ is the permittivity of polymer j relative to air,

$$\sigma = \frac{\sigma_2}{\sigma_1} \qquad \text{and} \qquad \eta = \frac{\eta_2}{\eta_1} \qquad (5)$$

are the ratios of surface tensions and bulk viscosities, respectively. The time integration of this system of equations is performed using an exponential propagation scheme[38] which may reliably be applied to thin film equations[39,40]. The non-dimensional system can formally be written as

$$\partial_{\widetilde{t}}\widetilde{h}_j = F_j(\widetilde{h}_1,\widetilde{h}_2). \qquad (6)$$

The linear stability of the steady films of constant thicknesses $\widetilde{h}_j = \widetilde{H}_j$ is determined by a spectral analysis of the Jacobian matrix $\mathbf{J}_{\widetilde{k}}$ of F. Since the problem is invariant under the planar Euclidian symmetry group, the linear system of equations can be solved independently for each Fourier mode, the general solution being the sum of all the modes. In other words, Eqs. (6) may be studied using the ansatz

$$\widetilde{h}_j(\widetilde{\mathbf{r}},\widetilde{\mathbf{k}}) = \widetilde{H}_j + \xi\chi_j\exp\left(\beta\widetilde{t} + i\widetilde{\mathbf{k}}\cdot\widetilde{\mathbf{r}}\right)$$

Each Fourier mode then obeys the eigenvalue equation $\beta(\widetilde{k})\boldsymbol{\chi} = \boldsymbol{J}_{\widetilde{k}}\cdot\boldsymbol{\chi}$. Its solution gives the dispersion relation $\beta(\widetilde{k})$, and the eigenvector $\boldsymbol{\chi}$ with components χ_j with $j=1,2$. With the proper normalisation, one may write the eigenvector as $\boldsymbol{\chi} = (1,\chi)$ where χ represents the amplitude ratio of the perturbations of the polymer layer one and two. The sign of χ determines whether the eigenmode is a mirror mode $(+)$ or a zig-zag mode $(-)$. In the following, we focus on the non-dimensional system Eqs. (4) and drop the tildes.

This journal is © The Royal Society of Chemistry [year]

3.2 Stability analysis

3.2.1 Jacobian

To study the linear stability with respect to each Fourier mode k we consider the Jacobian

$$\mathbf{J}_k = k^2 \mathbf{Q} \cdot \mathbf{E}$$

where the mobility matrix is

$$\mathbf{Q} = H_1^3 \begin{bmatrix} 1 & 0 \\ 0 & m \end{bmatrix}$$

and

$$m = \frac{m_2}{m_1} = \frac{\eta_1 h_2^3}{\eta_2 h_1^3} \tag{7}$$

is the mobility ratio of fluid 2 to fluid 1 with $m_j = h_j^3/\eta_j$. One also has the energy matrix in Fourier space

$$\mathbf{E} = -\mathbf{E}_0 - k^2 \begin{bmatrix} 1 & 0 \\ 0 & \sigma \end{bmatrix}$$

with

$$\mathbf{E}_0 = \begin{bmatrix} f_{11} & f_{12} \\ f_{21} & f_{22} \end{bmatrix}$$

where

$$f_{ij} = \partial_{h_i} \partial_{h_j} f_{el} = 2 \left(\frac{1}{\epsilon_i} - 1 \right) \left(\frac{1}{\epsilon_j} - 1 \right) f_{el}^3.$$

As a result,

$$\mathbf{J}_k = -H_1^3 k^2 \begin{bmatrix} 1 & 0 \\ 0 & m \end{bmatrix} \cdot \left(\mathbf{E}_0 + k^2 \begin{bmatrix} 1 & 0 \\ 0 & \sigma \end{bmatrix} \right). \tag{8}$$

Note, that as a consequence of the Euclidian plane invariance, the Jacobian is independent of the direction of the wavevector. Eq. (8) is used to determine the eigenvalues (growth rates β) and the eigenvectors (amplitude ratio χ).

3.2.2 Physical interpretation In order to better understand the physical meaning of the stability analysis, we focus on the particular case of two fluids with identical surface tensions and mobilities, namely [cf. Eqs. (5) and (7)]

$$\sigma = m = 1.$$

Under this assumption Eq. (8) becomes

$$\mathbf{J_k} = H_1^3 k^2 \left(-\mathbf{E}_0 - k^2 \mathbb{I}_d \right)$$

where $\mathbb{I}_d$ is the 2×2 identity matrix. The terms in parentheses are the linear contributions of the electric and Laplace pressure terms respectively. Obviously, the stabilizing Laplace pressure has the negative double eigenvalue $-k^2$. The fact that the eigenvalue is double is a consequence of the assumption of identical fluid properties. The electric pressure is the *only* destabilizing influence and so one expects that there is at least one positive eigenvalue of $-\mathbf{E}_0$. The computation of its eigenvalues β and the corresponding amplitude ratio χ gives

$$\begin{aligned} \beta_+ &= k_c^2 && \text{and} && \chi_+ = \frac{1}{\alpha} \\ \beta_0 &= 0 && \text{and} && \chi_0 = -\alpha \end{aligned}$$

with

$$\begin{aligned} k_c^2 &= -\operatorname{tr}(\mathbf{E}_0) \geq 0 \\ \text{and} \qquad \alpha &= \frac{\frac{1}{\epsilon_1} - 1}{\frac{1}{\epsilon_2} - 1} > 0. \end{aligned}$$

Note that from this definition of α

$$\epsilon_1 > \epsilon_2 \Leftrightarrow \alpha > 1.$$

These results may be understood by noting that the electric pressure becomes larger when the distance between the two liquid films decreases. Thus, the positive eigenvalue β_+ corresponds to the mirror mode ($\alpha > 0$). The presence of the zero eigenvalue is noteworthy but it may be explained in a similar way. If one increases the height of the flat film 1 by one unit and one decreases the thickness of film 2 by the factor α then the electric pressure is the same as for the unperturbed film. Indeed, that is a consequence of the following invariance property of f_{el}

$$f_{el}(h_1, h_2) = f_{el}\left(h_1 + u, h_2 - \alpha u\right) \tag{9}$$

where u is a perturbation. This property remains valid under differentiation, and so the matrix $\mathbf{E}_0$ also has it. Therefore, the zig-zag mode $(1, -\alpha)$ corresponds to the invariant direction, in other words, to the zero eigenvalue. This is the main difference between the present system and the two-layer systems studied in[26–28] where no such invariance property exists. In fact, the invariance directly results from the lack of a mechanical coupling between the two layers in our case (see section 3.1).

Next, we deduce the eigenvalues and eigenvectors of $\mathbf{J}$. If $\mathbf{P}$ is a matrix of the normalized eigenvectors of $\mathbf{E}_0$ then

$$\mathbf{J} \quad = \quad \mathbf{P} H_1^3 k^2 \begin{bmatrix} k_c^2 - k^2 & 0 \\ 0 & -k^2 \end{bmatrix} \mathbf{P}^{-1}$$

Then, the eigenvectors of $\mathbf{J}$ are identical to the ones of $\mathbf{E}_0$ and

$$\begin{aligned} \beta_+(\mathbf{J}) &= H_1^3 k^2 \left(k_c^2 - k^2 \right) && \text{and} && \chi_+ = \frac{1}{\alpha} \\ \beta_-(\mathbf{J}) &= -H_1^3 k^4 && \text{and} && \chi_- = -\alpha \end{aligned}$$

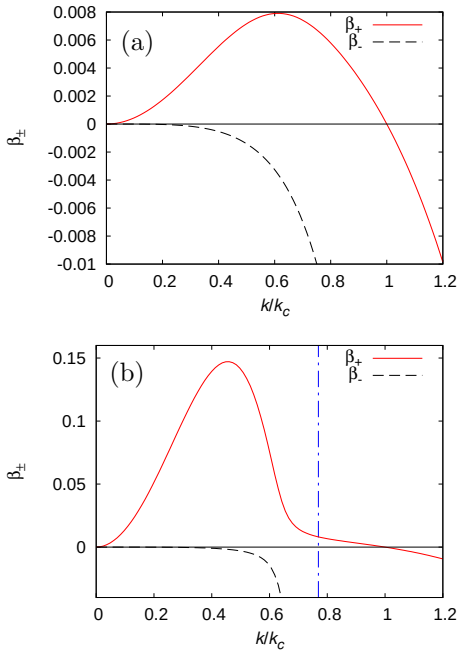


Fig. 2 Examples of growth rate $\beta_\pm$ for two systems (a) PS100-PS100 and (b) PMMA100-PS100. In both cases β_+, corresponding to the mirror mode, is unstable and grows in time for wavenumbers below k_c or k/k_c below 1. The rescaled wavenumber $k_{\max}/k_c$ that corresponds to the maximum of β_+ dominates the features in the profiles (a and b). The vertical dash-dotted line in (b) indicates where the band of weakly unstable wavenumbers starts (Eq. (14)).

Note, that the factors χ are entirely determined by α, i.e. by the dielectric properties. Moreover, the zig-zag mode is always stable. This is easy to understand knowing that the Laplace pressure stabilizes the film and the electric pressure for this mode is neutral due to the invariance property of Eq. (9). For the mirror mode the dispersion relation is that of the one-layer problem with the critical wave number given by

$$k_c = \sqrt{-\operatorname{tr}(\mathbf{E}_0)}. \tag{10}$$

Note, in particular that the maximal growth rate $\beta_{\max}$ is obtained for

$$k_{\max} = \frac{k_c}{\sqrt{2}} \tag{11}$$

and

$$\beta_{\max} = \frac{1}{4} H_1^3 \sqrt{-\operatorname{tr}(\mathbf{E}_0)}$$

The above results are reminiscent of the one-layer problem where $\operatorname{tr}(\mathbf{E}_0)$ is related to the second derivative of the free energy [17,21]. Here, however, $\mathbf{E}_0$ depends on both film thicknesses.

In the general case, where the condition $m = \sigma = 1$ is relaxed, one cannot deduce the eigenvectors of $\mathbf{J}$ from those of $\mathbf{E}_0$. The dispersion relation of each mode for the specific experimental cases where $m = 0.130$ and $m = 0.012$ are presented in Fig. 2a and Fig. 2b, respectively. More results are given in appendix A. Mirror and zig-zag modes are still found with the zig-zag mode being unconditionally stable while the mirror mode is unstable for $0 < k \leq k_c$ where the critical wavenumber k_c obeys Eq. (10) independent of the viscosity of the fluids. In addition to the dependence on the dielectric properties α, the most unstable wavenumber for the mirror mode (and the corresponding χ) also depends on the mobility ratio m, and surface tension ratio σ. This implies that the ratio of the growing roughnesses of the two interfaces (equivalent to the ratio of the growing amplitudes of the mode with the fastest growing wavenumber) and the spatial patterns depend on m, σ, and α, but not on the capacitor properties U and d. The conclusion is that m, σ, and α determine the qualitative properties in the linear growth regime, while the other parameters, in particular, U and d only enter length and time scales.

3.2.3 Limiting cases $m \ll 1$ and $m \gg 1$ In the experiment, the mobility ratio m may differ significantly from one. Next, we study the limiting case where $m \ll 1$. For $m = 0$ film 2 remains flat and one finds that

$$k^0_{\max} = \frac{k_c}{\sqrt{2}} \sqrt{\frac{\sigma\alpha^2}{\sigma\alpha^2+1}} < \frac{k_c}{\sqrt{2}}, \tag{12a}$$

$$\beta^0_{\max} = \frac{1}{4} H_1^3 k_c^4 \left(\frac{\sigma\alpha^2}{\sigma\alpha^2+1} \right)^2, \tag{12b}$$

$$\chi^0_{\max} = 0. \tag{12c}$$

where the superscript "0" indicates that $m = 0$.

A first order approximation of $\chi_{\max}$ for small $m \ll 1$ is

$$\chi_{\max}(m) = \frac{2m}{\alpha} + O(m^2) \tag{13}$$

It is noteworthy that, to a first order approximation, the amplitude ratio does not depend on the relative surface tension σ.

For $m = 0$, the complete dispersion relation of the unstable mode becomes

$$\beta^0_+(k) = H_1^3 k^2 \begin{cases} \left(\frac{\sigma\alpha^2}{\sigma\alpha^2+1}\right) k_c^2 - k^2 & \text{if} \quad k < \zeta k_c \\ 0 & \text{if} \quad \zeta k_c \leq k \leq k_c \end{cases}$$

with

$$\zeta = \sqrt{\frac{\sigma\alpha^2}{\sigma\alpha^2+1}} \tag{14}$$

This journal is © The Royal Society of Chemistry [year]

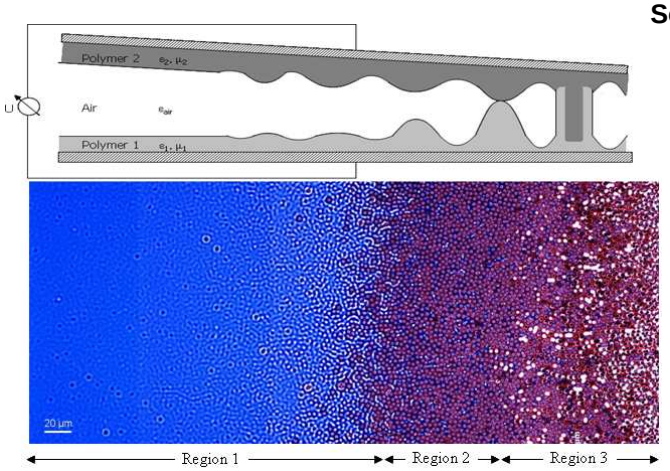


Fig. 3 Schematic of polymer-air-polymer system together with optical micrographs showing the structures formed by one of the polymer layers. The polymer film thicknesses are $h_1 = 322$ nm and $h_2 = 163$ nm and $M_w = 100$ kg/mol. The angle between capacitor plates is strongly exaggerated for illustration purposes.

i.e. for $k < \zeta k_c$, the dispersion relation is a 4^{th} degree polynomial reminiscent of the one for the single layer system. However, the growth rate is near zero in the adjacent band of wavenumbers $\zeta k_c < k < k_c$. In consequence, at small m the latter band becomes a weakly unstable band with growth rates that are much smaller than the ones for $k < \zeta k_c$. In practice this means that patterns with wavenumbers $\zeta k_c < k < k_c$ will nearly not develop. This might result in more regular patterns because some shorter wavelengths do not appear. This suppression of large unstable wavenumbers can be seen clearly in the dispersion relation in Fig. 2b.

The limiting case $m \gg 1$ is closely related to the limit $m \ll 1$, as only the roles of the two liquid layers are exchanged. This implies that the relations given above for the $m \ll 1$ case directly apply if one replaces α and σ by $1/\alpha$ and $1/\sigma$, respectively. In general, for any $m > 1$ one can map the system onto a system with $m < 1$ by reversing the role of the two individual layers.

4 Results

4.1 Influence of variation in gap width

Experimentally, different stages in the development of a polymer film instability are simultaneously observed in a given polymer-air-polymer experiment. The two electrode plates are never perfectly parallel, but are inclined with respect to each other by a small angle (see upper part of Fig. 3). In consequence, there exists a gradual spatial change in the electric field between the electrodes that leads to a gradual spatial change in the local growth rate of the instability. According to the scaling (Eq. (3) and appendix A), the variation δd in the gap width d does not influence the amplitude ratio χ, but rather the maximal growth rate $\beta_{\max}$ and the wavenumber $k_{\max}$. Their relative variations are given by

$$\frac{\delta\beta_{\max}}{\beta_{\max}} = 2\frac{\delta k_{\max}}{k_{\max}} = -\frac{6}{d + h_1(\frac{1}{\bar{\epsilon}_1} + 1) + h_2(\frac{1}{\bar{\epsilon}_2} + 1)}\,\delta d. \tag{15}$$

The relative variation of $\beta_{\max}$ is twice that of $k_{\max}$. Both increase linearly when the plates get closer. Note however, that the linear increase in $\beta_{\max}$ actually corresponds to a linear increase in the rate of exponential growth, i.e., it will result in an exponential variation δa_j of the amplitude a_j of the observed pattern in the film j:

$$\frac{\delta a_j}{a_j} = e^{\delta\beta t} - 1$$

For a particular time t, the change in structure height in the direction of decreasing gap width is qualitatively similar to the observed change in time for ideally parallel plates. However, if the exact slope of the gap is not known, it is impossible to deduce the growth rate $\beta_{\max}$ from the observation of the gradual spatial change. The lower part of Fig. 3 shows a typical example of the effect of this wedge geometry in an optical microscopy image of one layer from a PS100-PS100 system ($m = 0.130$, $\alpha = 1$, $\sigma = 1$, $\eta = 1$, $h_1 = 322$ nm, $h_2 = 163$ nm). The sketch in the upper part of Fig. 3 illustrates the spatial variation of the growth of the instability that results from the small angle between the plates. At the centre of the sample where the plate separation is large and the electric field is low (Fig. 3, Region 1), an early stage labyrinthine surface topography is observed. The gap decreases towards the right edge of the sample (Fig. 3, Region 2), giving rise to an increased electric field. This results in more developed column-like structures. In Region 3 of Fig. 3 the structures from both films are in contact marking the final stage of development. The white spots correspond to column structures that had been in contact and were removed from the imaged film when the two capacitor plates were mechanically separated for analysis.

4.2 Mirror mode

The evolution of the instability in the two films can be numerically simulated using Eqs. (4). Random small surface corrugations (due to thermal noise) are added to the flat film profiles to initialize the instability in the simulations. Note, however, that no further noise is added

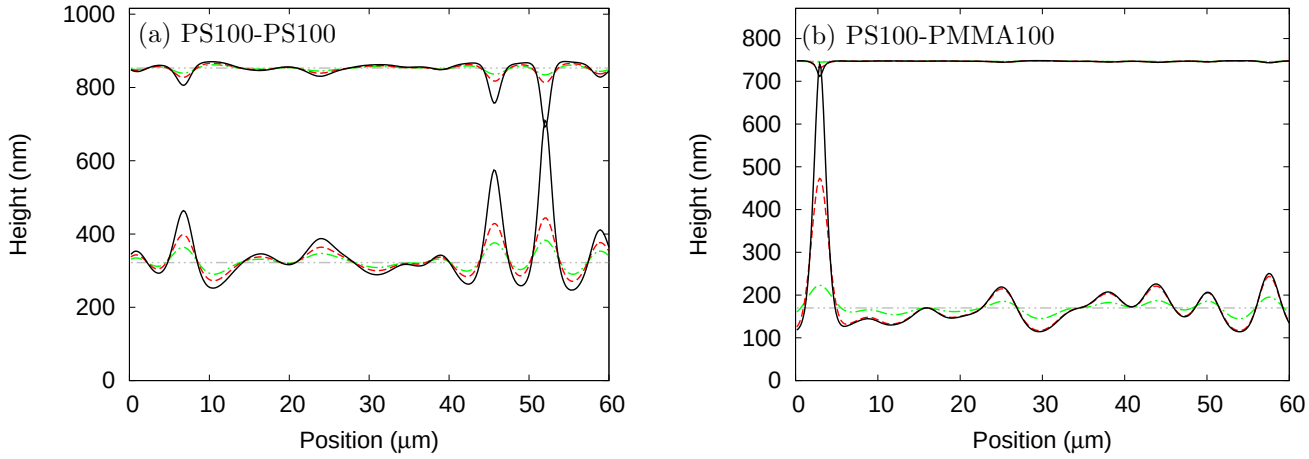


Fig. 4 (a) Snapshots of 2d slices from 3d simulations for different times of the pattern evolution of (a) PS100-PS100 ($m = 0.130$, $\eta = 1$, $\alpha = 1$) and (b) PS100-PMMA100 ($m = 0.012$, $\eta = 34$, $\alpha = 0.83$). The profiles of the two PS100 layers in (a) with thicknesses $h_1 = 322$ nm (bottom) and $h_2 = 163$ nm (top) are given for times 0 s, 128 s, 135 s, and 141 s. The substrate separation was $d = 1016$ nm. The profiles of PS100 ($h_1 = 170$ nm; bottom film) and PMMA100 ($h_2 = 124$ nm; top film) in (b) are given for times 0 s, 875 s, 971 s, and 978 s. The substrate separation was $d = 870$ nm.

throughout the simulation. In agreement with the linear analysis, we find that only the mirror mode develops and a zig-zag mode is not observed. Figure 4 presents snapshots of two-dimensional slices through the films that are made at different times as the instability evolves, whereas Figure 5 gives such snapshots of the full surface topography. Finally, Figure 6 shows the surface topography at the final stage, i.e., when features of both films touch each other for the first time.

When the polymers in the two layers in a polymer-air-polymer experiment have the same molecular weight (e.g. PS100-PS100) and therefore the same bulk viscosity, but differing film thicknesses ($m = 0.130$), as shown in Fig. 7a, the surface patterns of the two layers form mirror images. This mirroring of the surface topography is also seen when the mobility ratio m is increased ($m = 0.260$) and different polymer pairings ($\alpha = 1.20$) are used as in the case of PMMA10-PS150 shown in Fig. 8a. Due to the slight angle between the electrodes (see section 4.1), different stages of film evolution are observed on a single sample. Nevertheless, taking relative feature height as a distinguishing factor, the two surface profiles are clearly seen to mirror each other. As predicted by the theoretical model the observed modes are mirror modes and no zig-zag mode is observed for the various parameter sets (m and α) used in the experiments. Decreasing m also leads to mirroring as discussed in section 4.4.

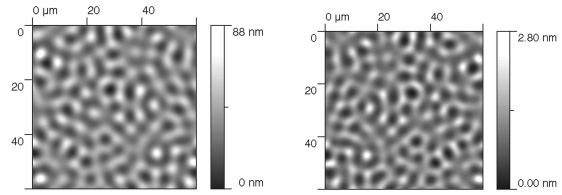
4.3 Wavelength of instability modes

The dispersion relation for the polymer-air-polymer system (derived in the appendix, see Eq. 19) is plotted in Figs. 2a and 2b for our experimentally used PS100-PS100 and PS100-PMMA100 systems, respectively. Note that the mirror (β_+) and zig-zag (β_-) modes are exponentially amplified (continuous lines), and damped (dashed line), respectively. The mirror mode is unstable in the wavenumber range $[0, k_c]$ with k_c given in the appendix by Eq. (21).

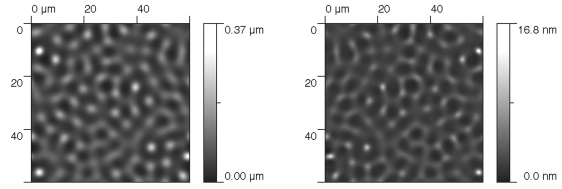
The maximum of the growth rate of the mirror mode corresponds to the fastest growing mode, and the corresponding wavenumber is expected to dominate the film pattern. The scaled wavenumber $k_{\max}$ of the fastest growing mode can be extracted by numerically solving Eq. (22) (appendix) and considering the real solutions with $k > 0$. The value of α is estimated to lie for common polymers within the interval $[0.6, 1.6]$. In Fig. 9a, the scaled wavelength $\lambda_{\max} = k_c/k_{\max}$ is plotted for three values of α, and $0 \leq m \leq 1$. In all cases $\sigma \simeq 1$ is assumed. A single unstable mode is found to dominate the system over this range.

In all experiments, one observes a mirror mode with a clearly dominant wavelength that is constant (within experimental error $\leq 10\%$) over square areas with side lengths 100 μm $\leq L \leq$ 600 μm. This is partly due to the fact that the pattern wavelength is much less sensitive to variations in the gap width than the amplitude of the pat-

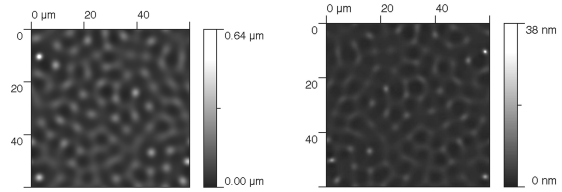
 This journal is © The Royal Society of Chemistry [year]



(a) PS100, $t = 874$ s **(b)** PMMA100, $t = 874$ s

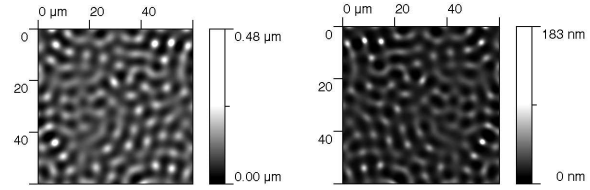


(c) PS100, $t = 971$ s **(d)** PMMA100, $t = 971$ s

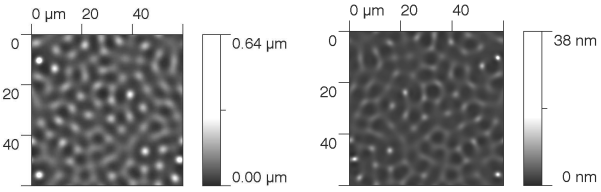


(e) PS100, $t = 978$ s **(f)** PMMA100, $t = 978$ s

Fig. 5 Snapshots of the evolving topography of the PS100-PMMA100 system obtained via time simulation (see caption of Fig. 4b).



(a) PS100, $h_1 = 322$ nm **(b)** PS100, $h_2 = 163$ nm



(c) PS100 **(d)** PMMA100

Fig. 6 Simulated surface topography at the time of first contact between the films PS100-PS100 (a) and (b), and PS100-PMMA100 (c) and (d) (see caption of Fig. 4).

terns[41] (see section 4.1). To compare the experimental results with the theoretically obtained wavelength $\lambda_{\max}$, we rescale the measured experimental wavelengths $\lambda_{\exp}$ from studies in which the gap width d can be estimated by

$$\lambda = (\lambda_{\exp}\lambda_{el}^{\frac{1}{2}}k_c)/d^{\frac{3}{2}} \tag{16}$$

using the scales Eq. 3 and k_c given by Eq. (21).

To calculate λ it is necessary to know the gap width d between the plates. An experimental approach is used to estimate it. By measuring the feature heights in regions that are fully developed and almost in contact (transition area between region 2 and region 3 in Fig. 3), one can estimate d as being at least equal to the sum of these heights of the two films ($d = h_{1s} + h_{2s}$, Fig. 9a). In fact, this is an underestimate since there will always be a thin residual layer underneath the columnar structures, i.e., the real plate separation is slightly larger than the estimated one. Nevertheless, the scaled experimental wavelengths match the corresponding theoretical predictions within experimental uncertainty (Fig. 9a).

An overestimate forms a second bound by assuming that the structures develop on top of the initial film thickness h_j. The resulting estimate is $d = h_{1s} + h_{2s} + h_1 + h_2$. For each of the two obtained values for d, the corresponding wavelength is calculated employing Eq. (16). In Fig. 9b both, the underestimates and overestimates of λ are presented. They clearly bracket the theoretical curve $\lambda_{\max} = k_c/k_{\max}$ with λ based on $d = h_{1s} + h_{2s}$ being closest. Thus, using exact measurements of the gap width, the theoretical model should correctly predict the experimentally observed wavelength. To test this further, we measure the wavelengths in additional experiments (not presented), and extract the gap width in 9 additional cases by fitting λ to $\lambda_{\max}$ (Fig. 9a). The gap width is found to lie between 460 nm and 930 nm, an acceptable range for a wedge-shaped gap that is created by 1 µm spherical spacers that separate the substrates on a lateral length scale in the millimetre range.

As shown in Fig. 9, the wavelength of the instability $\lambda_{\max} = k_c/k_{\max}$ depends on the mobility ratio m, and thus for fixed film thicknesses on the ratio of viscosities. Note that we use the bulk viscosity values in the calculation of $\lambda_{\max}$. Recently, a reduction of the viscosity in thin polymer films as compared to the bulk value has been discussed for polymers of high molecular weight[19]. The effect results from non-equilibrium conformations of the chains in as-cast films, i.e., frozen-in in-plane stresses. However, here such an effect does not seem to influence the linear behaviour that selects the fastest wavelength as our theoretical prediction of the wavelength agrees within the error ($\leq 10\%$) with the experimentally measured one.

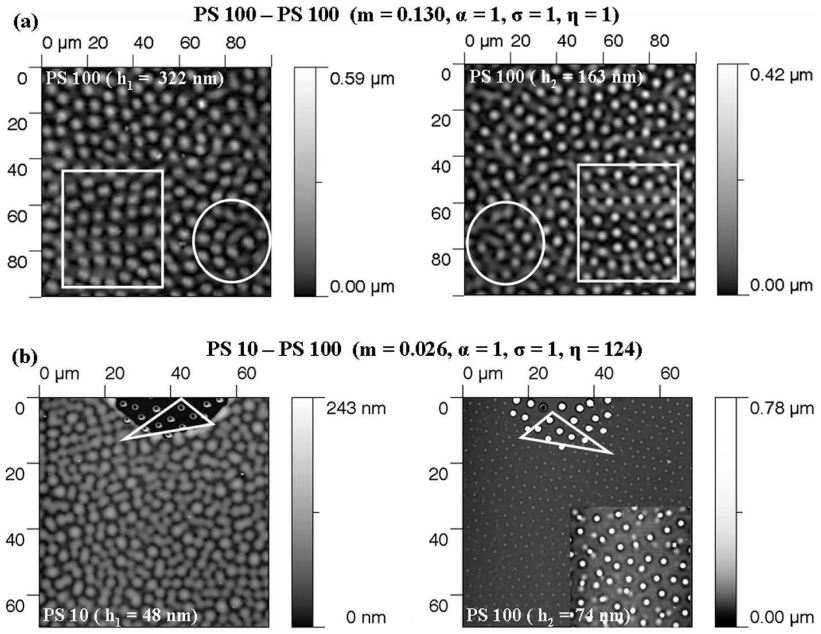


Fig. 7 AFM images of the surface topography and the mirror pattern formed in a polymer-air-polymer system caused by an electric field induced instability for two polymer films with the same dielectric constant (PS-air-PS). A decrease in the mobility ratio m leads to a change in surface topography. The geometrical shapes formed by white lines are used to emphasize mirrored patterns. The inset in the lower right corner of the PS100 AFM image shows $\approx$ 3 to 10 nm lower height satellites (1 to 3 in number) surrounding $\approx$ 26 to 32 nm high drop-shaped structures. The threshold height limit in this inset is 20 nm.

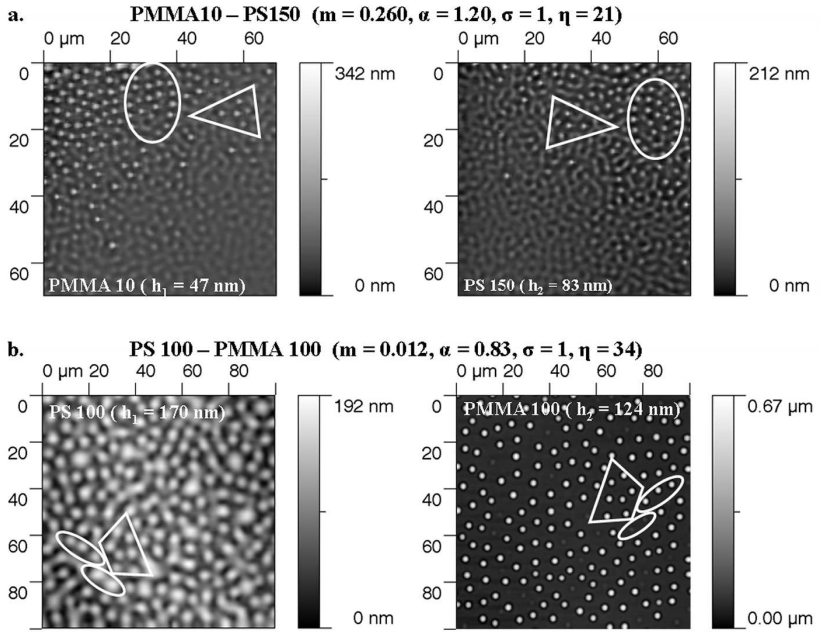


Fig. 8 AFM images for the case where the two films have different dielectric constants (PS-air-PMMA). A decrease in m leads to a change in surface topography similar to that observed in Fig. 7.

 This journal is © The Royal Society of Chemistry [year]

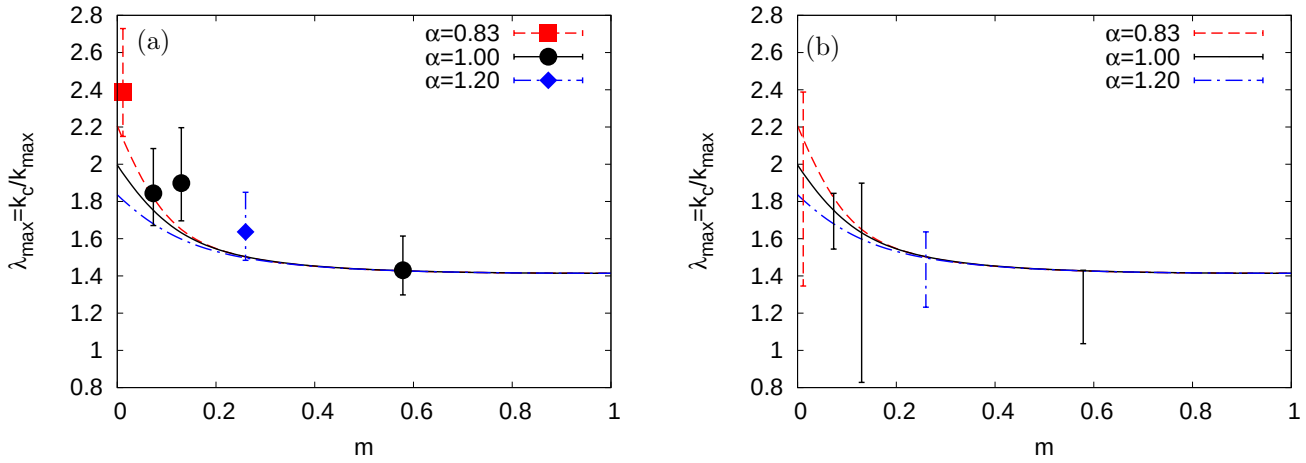


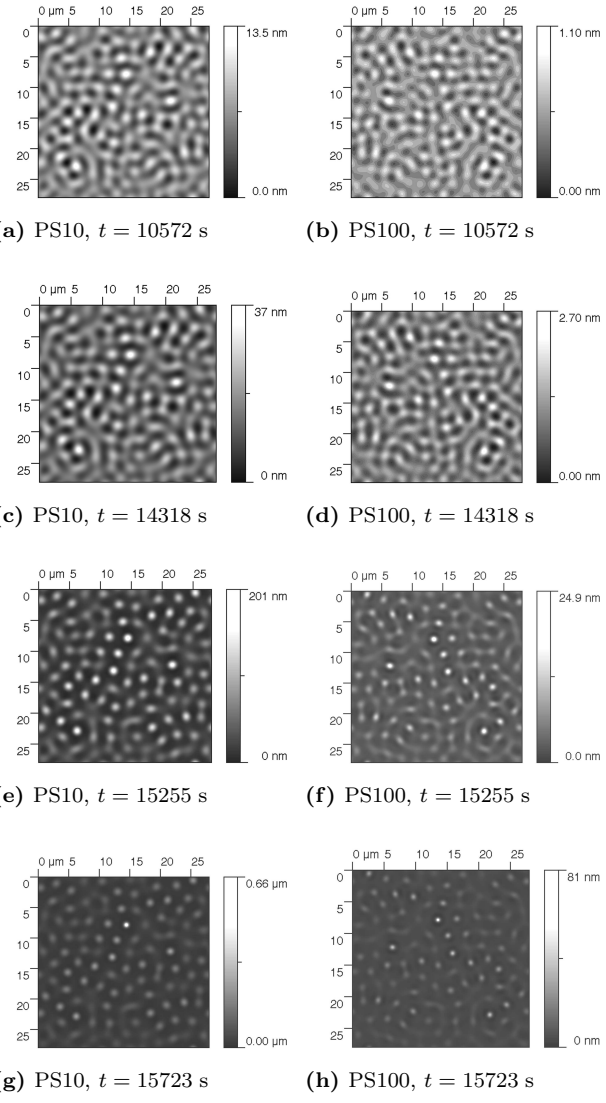
Fig. 9 Scaled wavelength $\lambda_{\max} = k_c/k_{\max}$ as a function of the mobility ratio m for the three experimentally studies values of the permittivity parameter α. (a) Experimentally measured wavelength λ (symbols) scaled according to Eq. (16) and uncertainties using an underestimate of the substrate separation d. (b) λ using an overestimate and underestimate (denoted by the lower and higher errorbars) of the substrate separation. The theoretically expected $\lambda_{\max} = k_c/k_{\max}$ as a function of m for indicated values of α are shown as lines.

Theoretical and measured values also agree within experimental error independently of the used M_w of the polymers, and there is no systematic shift with M_w in the observed differences. However, such an effect might be visible in the nonlinear behaviour when the film thickness becomes locally much thinner than the original height of the initial flat films.

4.4 Topography

The final stage of the simulated evolution is reached when features in the top and bottom films touch for the first time. Corresponding profiles for the PMMA100-PS100 system ($m = 0.012$, $\alpha = 0.83$, $\sigma = 1$) are presented in Figs. 6c and d as top views. Inspection reveals a mainly labyrinthine topography for both surfaces with a few more column-like structures, e.g., in the lower right corner of Figs. 6c, mirrored in the lower left corner of Figs. 6d. Such a labyrinthine topography is seen for all studied sets of experimental parameters (m, α and σ) in the early simulation stages, i.e., when the behaviour is mainly linear. Experimentally, we see such mirrored labyrinthine topographies in all of the studied cases with m larger than 0.1. Labyrinthine patterns are clearly visible for PS100-PS100 ($m = 0.130$, $\alpha = 1$) in region 1 of Fig. 3. At a more developed stage in Fig. 7a individual drop-shaped protrusions (drops) start to dominate this pattern in both films at the same time. The mirrored labyrinthine topography is also visible in the PMMA10-PS150 system ($m = 0.260$, $\alpha = 1.20$) shown in Fig. 8a as is also the transition to more developed drops.

However, the experimentally observed topography in the two polymer layers is radically different when the mobility ratio is decreased by using polymers with very different viscosities. In Fig. 7b, we decrease the m value to 0.026 by using PS10-PS100. Then, the higher mobility film (PS10, $h_1 = h_{\mathrm{PS10}} = 48$ nm) exhibits structures of ≈ 80 nm amplitude that resemble the familiar labyrinthine pattern even though the tendency towards a pattern of drops is already developed. The lower mobility film (PS 100, $h_2 = h_{\mathrm{PS100}} = 74$ nm) exhibits isolated drops of ≈ 30 nm amplitude. The patterns in the two films still mirror each other, i.e., the locations of the maxima agree even if overall the film topographies look different. A close inspection of the PS100 layer reveals that in the vicinity of the higher drops there exist small satellite droplets of ≈ 3 to 10 nm amplitude. They are clearly visible in the inset to Fig. 7b that is created employing a lower height threshold (see also Fig. S1[42]). Indeed, it is the combination of the drops and their satellites in the PS100 film that corresponds to a mirror feature in the PS10 film. The measured amplitude ratio, ≈ 0.04 to 0.13, between the satellite drops in the PS100 (≈ 3 to 10 nm) and the PS10 structure (≈ 80 nm) is consistent with the amplitude ratio, ≈ 0.05, calculated using Eq. (13) obtained from the linear analysis. This implies that the linear theory predicts a structure height similar to that of the satellite droplets in the PS100 film, but it does



(a) PS10, $t = 10572$ s **(b)** PS100, $t = 10572$ s

(c) PS10, $t = 14318$ s **(d)** PS100, $t = 14318$ s

(e) PS10, $t = 15255$ s **(f)** PS100, $t = 15255$ s

(g) PS10, $t = 15723$ s **(h)** PS100, $t = 15723$ s

Fig. 10 Simulated topography evolution of the PS10-PS100 sample (see Fig. 7 for experimental details).

not predict the presence of the observed isolated drops of much greater height. This suggests that the latter results from the nonlinear stage of evolution. An inspection of Fig. 10, however, shows that the corresponding nonlinear simulation does not exhibit structures consisting of main and satellite droplets. Therefore, it seems that some aspects of the nonlinear evolution are not captured by the model.

The distinctive asymmetry in the topography of the films and the mismatch between simulations and experiment is also found using different polymers, e.g., for the PS100-PMMA100 system ($\alpha = 0.83$, $m = 0.012$) shown in Figs. 4b, 5, 6c and 6d (simulation) and Fig. 8b (experiment). Further analysis (Fig. S2[42]) reveals that rims of 4 to 7 nm amplitude surround the higher isolated drops in PMMA. Using the amplitude ratio predicted by linear theory i.e. Eq. (13), features of ≈ 4 nm are expected. The simulation does not show however the experimentally observed stark difference between a labyrinth-type pattern in one film and high isolated drops in the other film. This reinforces the impression formed above that the nonlinear description is incomplete. The discrepancy becomes larger at a later stage of the evolution where one actually finds the opposite ratio of feature heights in the simulation as compared to the experiment: In the simulation the PS100 film ($h_1 = h_{\mathrm{PS100}} = 170$ nm) shows much larger feature heights of ≈ 640 nm compared with ≈ 38 nm for the PMMA100 film ($h_2 = h_{\mathrm{PMMA100}} = 124$ nm), consistent with the linear result. The opposite trend is found in the experiment where the feature heights in the PS100 and PMMA100 layers are respectively ≈ 150 nm and 570 nm.

To summarise, when the mobility ratio m is larger than a threshold value m_c that lies between 0.03 and 0.1, mirrored labyrinthine patterns (in different evolution stages) are observed in the two films. We will refer to this as a Type I behavior. When m is smaller than m_c, the lower mobility film exhibits isolated drops, with either surrounding satellite droplets or rims of low height, while the higher mobility film shows labyrinthine patterns regardless of film thickness and α. We will refer to this as Type II behavior. Note that in this paper the ordering of films is selected to ensure $m = m_2/m_1 \leq 1$, i.e., the film with lowest mobility is always defined as film 2: If one relaxes this constraint then by symmetry Type I behavior will also occur for $1 \leq m \leq 1/m_c$ and Type II behaviour when m is greater than $1/m_c$.

We conclude that the mobility ratio m determines the topography of the films and the type of behavior observed in the evolution of the structure. The dielectric properties of the film do not seem to affect their topography, both types of behavior are equally observed for different values

 This journal is © The Royal Society of Chemistry [year]

of α.

In addition to the evidence gathered from the inspection of the snapshots that led us to distinguish Type I and II behaviour, the effect can be further quantified by an analysis of the surface topographies. Fig. 11(a) and (c) show the cumulative distributions of normalised heights for two film thickness profiles for the PS100-PS100 and PS10-PS100 system, respectively. The data in these figures are normalized to have a mean of zero and a standard deviation of one. This allows comparison of the functional form of the statistical distributions. Differences are indicative of differing film topographies.

From Fig. 11a, it is clear that the functional forms of the two PS100 layers ($m = 0.130$, $\eta = 1$) are in agreement with each other, while in contrast for smaller m (Fig. 11c) the functional forms of the PS10 and PS100 films ($m = 0.026$, $\eta = 124$) differ. This confirms quantitatively that the two films are similar for Type I behaviour and different for Type II behavior as qualitatively discussed above for corresponding AFM images in Fig. 7. In addition to the cumulative distributions obtained from the experimental data, the figure gives the distributions for the final stage of the corresponding simulations and also a normal distribution for reference. One notes that the functional forms for experiment and simulation agree in the case of the PS100-PS100 system corroborating that the model correctly predicts the surface topographies for higher $m \approx 0.1$. The distributions do, however, not agree in the case of the PS10-PS100 system confirming the above described difference between simulation and experiment when m is less than some threshold value m_c somewhere between 0.03 and 0.1 (or equivalently greater than $1/m_c$).

Type I and Type II behavior is also found from the experimental data of the PMMA10-PS150 system ($m = 0.260$, $\eta = 21$), and the PS100-PMMA100 system ($m = 0.012$, $\eta = 34$), respectively, when analysing the cumulative distribution of normalised heights (Fig. 8 and Fig. S3[42]). The transition from Type I to Type II behavior occurs as the mobility ratio m is decreased.

In all studied experiments the peaks in the patterns are always mirrored and the corresponding columns come into contact when they are fully developed even where the surface topography is different in the two films. This confirms the prediction of the linear analysis that the instabilities in the two films are coupled and the system exhibits only a mirror mode. At a later stage, the nonlinear model predicts well the behaviour for mobility ratios close to one (Type I), but fails to show important aspects when m is much smaller (or larger) than one (Type II). In particular, the simulations do not show the strongly peaked rather isolated drop-shaped structures, although,

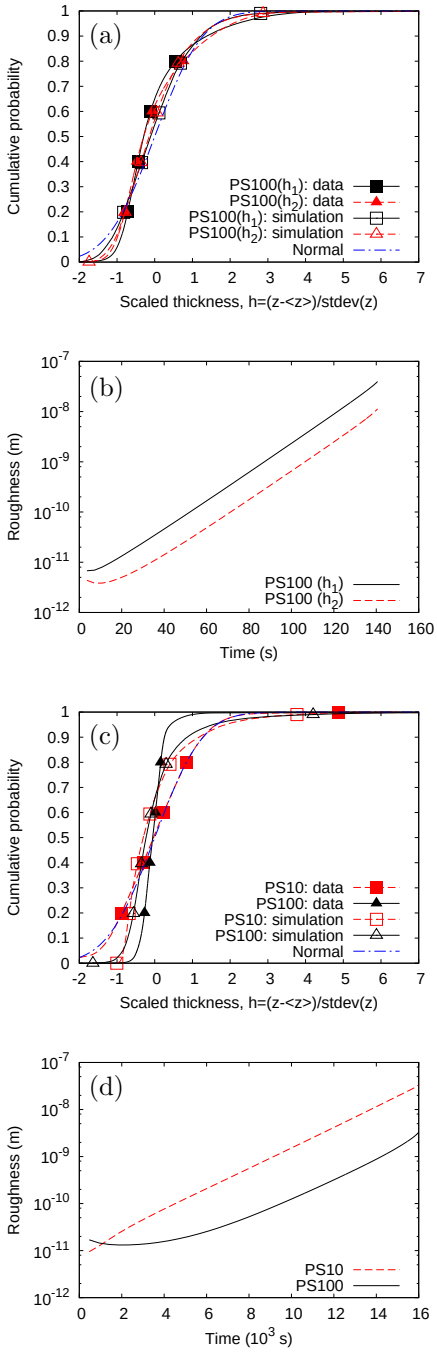


Fig. 11 The cumulative distributions of the film thicknesses for experiment and simulation in (a) PS100-PS100, and (c) PS10-PS100 systems. The cumulative distributions have been normalized such that their mean is zero and their standard deviation allows one to directly compare the forms of the distributions. The time dependence of the roughness of each film as predicted by the 3d model is presented in (b) for PS100-PS100, and (d) for PS10-PS100 systems.

excluding these, linear stability analysis does predict the ratio of feature heights experimentally observed in the films. These issues are further investigated in the following sections and a discussion of possible reasons is provided in the conclusion.

4.5 Growth rates

It has been shown theoretically that in the linear regime the amplitude ratio of the dominant mode only depends on the film parameters m, α, and σ. For the experiments presented, linear analysis predicts (using Eq. (20)) that the more mobile film has a greater instability amplitude. The unstable growth of the film roughness (see Eq. (1)) in time, obtained from simulations of the PS100-PS100 system (different film thicknesses) and the PS10-PS100 system (different film thicknesses and viscosities), is shown in Figs. 11b and 11d, respectively. Excluding the start of the simulations (where artificial noise is dominant) the films of highest mobility PS100 (h_1) in the PS100-PS100 system (Fig. 11b) and PS10 in the PS10-PS100 system (Fig. 11d) are always the roughest. At all times, the film of higher mobility therefore exhibits features of larger amplitude, regardless of whether the higher mobility $m_1 = h_1^3/\eta_1$ is a result of greater thickness (PS100-PS100) or lower viscosity (PS10-PS100). The ratio of roughnesses remains constant in time after an initial transient. Further examples that confirm this trend are shown in Figs. S3b and d[42].

Although the topography of the surfaces has been shown to clearly depend on m, the experimental dependence of the growth of the instability on m is more complex. In the PS10-PS100 system ($m < m_c < 1$), the roughness of the PS10 film is greater than that of the PS100 film(Fig. 12b). As the PS10 film has a higher mobility compared to PS100, this agrees with the simulation results in the linear and nonlinear phase. For the PMMA10-PS150 system ($1 > m > m_c$) the roughness of the PMMA10 film is approximately equal to the PS150 film during the early stage and greater during the late stage (Fig. 12c). This also agrees qualitatively with our theoretical prediction and simulation. Agreement in both cases however, occurs irrespective of whether the instabilities develop Type I (with $1 > m > m_c$) or Type II (with $m < m_c < 1$) behaviour.

Remarkably, the roughness ratio changes across the sample, i.e. during the time evolution of the PS100-PS100 and the PS100-PMMA100 systems. Depending on the spatial position on the sample (i.e. the phase of evolution) the higher mobility PS100 films, either have a smaller or larger roughness than the layer of lower mobility (the 163 nm PS100 film in Fig. 12a and the 124 nm PMMA100 film in Fig. 12d). Translating the spatial change across the sample into a time sequence implies that in both cases it is the film of higher mobility that has the larger roughness during the early stage of the time evolution whereas the opposite is true at later stages. The early time behaviour is in qualitative agreement with the linear analysis and time simulations, but the late time behaviour does not agree with the model (see for example, Fig. 11b and Fig. S3d[42]). The time simulations never show such a crossover in the roughness ratio between early (linear) and late (nonlinear) stages. Crossover also occurs regardless of whether Type I or Type II behaviour is exhibited.

A common factor in the remarkable change in the evolution of the roughness, is that in both cases it is the thinner film which evolves to become the roughest, although it has the lower mobility. Indeed, also for the systems which are in qualitative agreement with theoretical prediction, namely the PS10-PS100 and PMMA10-PS150 pairings, the thinner film is the roughest. However, there it has the higher mobility. In summary, it appears that the instability growth in the thinner film can accelerate at later times beyond the growth rate in the thicker film. This implies that the absolute film thickness matters beyond its role in the mobility ratio m. Possible reasons are discussed below in section 5.

5 Discussion and Conclusions

We have studied the structuring process of thin liquid polymer films under the destabilizing influence of a dc electric field in a polymer-air-polymer configuration using theoretical and experimental approaches. Unlike other systems containing multilayer thin polymer films, this configuration exhibits only a mirror mode of the surface instability, whereas the zig-zag mode is always damped, which is also in agreement with the theoretical work of Srivastava et al.[34]. This is related to the fact that the two layers are only coupled energetically but not mechanically.

The topographies of the film surfaces can be tuned by varying the mobility ratio $m = \eta_1 h_2^3/\eta_2 h_1^3$ which in our experiments is dominated by the ratio of the bulk viscosities. Depending on m, we have identified two different types of resulting surface topographies. Type I behaviour is found for values of m in the range $m_c \leq m \leq 1/m_c$, with m_c between 0.03 and 0.1, where both films show labyrinthine patterns from which drop-shaped patterns evolve simultaneously. Type II behaviour is found at values of m outside this range (here primarily due to large differences in the bulk viscosities) where the less viscous film exhibits a labyrinthine pattern with the more viscous film displaying isolated drop-like features surrounded by

 This journal is © The Royal Society of Chemistry [year]

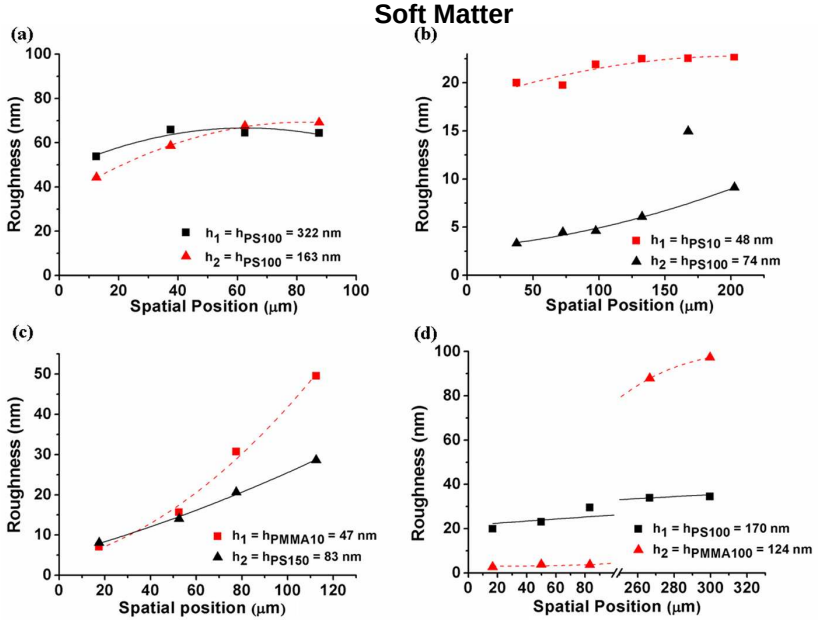


Fig. 12 The average roughness [Eq. (1)] of the polymer films as a function of the position measured across the sample corresponding to different d-spacings in the capacitor wedge geometry. Each point represents the roughness of a square area with side dimensions of, respectively, 25 μm (PS100-PS100), 35 μm (PS10-PS100), 35 μm (PMMA10-PS150) and 33.33 μm (PS100-PMMA100). The center of each area is taken as its position. All lines are guides to the eye. The roughness in (d) was measured in two separated regions and the position axis is broken to reflect this.

smaller secondary structures (satellite drops or a small circular rim).

A linear analysis of the employed long-wave model for the coupled evolution of the two film surfaces correctly predicts the occurrence of the mirror mode of the instability in the linear regime, its wavelength, growth rate and the amplitude ratio of the features in the two films. The nonlinear behaviour of the experimentally studied systems was theoretically investigated through time simulations of the nonlinear system of equations. They predict well the surface topography in the linear and nonlinear phase of evolution when m is in the range $m_c \leq m \leq 1/m_c$ (i.e. for similar film mobilities). The model is, however, unable to describe the topography that experimental systems show for small mobility ratios (i.e. Type II behaviour). Some experiments,irrespective of whether they exhibit Type I or Type II behaviour, show a subsequent crossover (in the nonlinear phase of evolution) where the film of lower mobility but also lower thickness develops the larger roughness. The time simulations of these cases do not show such a crossover in the roughness ratio between the early (linear) and the late (nonlinear) phases. In the theoretical work of Srivastava *et al.*[34] on a similar system, neither Type II nor crossover behaviours were reported. The topography and crossover results are summarised in Table 1.

An important assumption of the theoretical model is the validity of the long-wave approximation, which requires that the ratio of vertical and horizontal length scales is small everywhere, i.e. that surface slopes are small. To test whether this condition is met in all experiments at all stages, we have measured the slopes of the evolving peaks ∇h_i in each film at positions that correspond to early and late stage pattern development (Regions I and II in Fig. 3 respectively). During the early stage of pattern formation the slopes are $\nabla h_i \approx 10^{-2}$, fulfilling the condition for the long-wave approximation. During the later stages $\nabla h_i \approx 10^{-1}$ is one order of magnitude higher. The slopes are however still sufficiently small for the long-wave approximation to remain valid. Therefore, a breakdown of this approximation is an unlikely explanation for the qualitative discrepancies found between experiment and theory.

A consequence of the long-wave approximation is that the electric field only depends on the local distance between the two films but neither on the local slopes nor curvature of the surfaces. However, once the peak structures become sharper and ∇h_i increases beyond $\approx 10^{-1}$, curvature effects might become visible. A strongly curved charged surface gives rise to a contribution in the electric

Experiment name	h_1 (nm)	h_2 (nm)	m	α	σ	η	Topography Type	Growth crossover
PS100-PS100	322	163	0.130	1	1	1	I	yes
PS10-PS100	48	74	0.026	1	1	124	II	no
PMMA10-PS150	47	83	0.260	1.20	1	21	I	no
PS100-PMMA100	170	124	0.012	0.83	1	34	II	yes

Table 1 The experimental parameters for the film pairings in Figs. 7 and 8. For each pairing a summary is given of the topoography evolution type and occurrence of crossover in growth rates.

field which is proportional to the curvature[43]. Such a local enhancement of the electric field can accelerate structure growth even if the peak height is small. Our model does not take this into account. The resulting enhanced pressure at the interface of a more viscous film could effectively locally extrude perturbations in thin films.

Theoretically we have shown that the linear amplitude ratio is $\chi = 0$ for the limiting case of $m = 0$. This implies that for low m, where Type II behaviour is experimentally observed, the instability of the more mobile film is predicted to have a significantly greater amplitude than the less mobile. The observed normal distribution of film thicknesses of the more mobile PS10 film in the PS10-PS100 study (Fig. 11c) points to an equal distribution of heights at peaks and troughs. As seen experimentally, it is the more mobile film that always has the greater roughness during the initial stages. These observations support the view that peaks in the more mobile film impose the pattern upon the less mobile film. Note that this phenomenon is different from the case of imprinting a pattern via a patterned electrode[17,20], where the wavelength of the induced instability in the polymer film typically matches that of the pattern. In the polymer-air-polymer system the instabilities in the two films are always coupled, and the spatial locations of peaks in both films are mirrored from the onset. The wavelength is determined solely by the experimental parameters such as the mobility ratio (via the film thickness and viscosity), dielectric properties, surface tensions and the applied electric field. The position of the peaks is not controlled by this interplay, but rather the topography of the coupled mode is altered by varying the mobility ratio of the two layers.

We have noted that a common factor in the remarkable change in the evolution of the roughness or crossover is that the thinner film evolves to become the roughest, although it has the lower mobility. This might imply that the absolute film thicknesses matter beyond their present role in the mobility ratio m and that also the film viscosity is of larger importance than indicated by m. A possible explanation that involves both aspects would be that for very thin films the viscosities η_i themselves depend on film thickness. If such a dependence were stronger than h_i^3, the local effective m would be proportional to $(h_1/h_2)^\nu$ with $\nu > 0$ i.e. the dependence on film thicknesses would be inverted. The resulting dynamics can strongly differ from the one presented in our simulations that are obtained based on the assumption that the film viscosities always correspond to the bulk values, i.e., the mobility ratio m is a 'global' one.

The viscosity at the surface of a thin PS polymer film is thought to be smaller than in the interior of the film[44] and a reduction in thin film viscosity occurs for both low and high molecular weight PS if film thickness is reduced[45,46]. Based on a two layer model of thin film mobility in which the total mobility is the average of thickness dependent bulk and surface (m_s) mobilities[45,46], the effective viscosity of the film η_{eff} should decrease with thickness h from the bulk viscosity η according to $\eta_{\text{eff}} \simeq \frac{\eta h^3}{h^3+3\eta m_s}$, assuming a thickness of the surface layer $h_s \ll h$. Our model makes the assumption $h \gg h_c \equiv (3\eta m_s)^{\frac{1}{3}}$ where $\eta_{\text{eff}} \sim \eta$, i.e. it is constant. However, at thicknesses $h < h_c$, $\eta_{\text{eff}} \to \frac{h^3}{3m_s}$ and it is the mobility of the film that becomes constant. As a result a shallowing of the mobility is expected $m_j \sim h^{\nu_j}$, with ν_j decreasing from 3 to 0 as h_j decreases past h_c. The mobility ratio becomes $m = \frac{3m_{s,2}}{3m_{s,1}} \frac{\eta_2+h_2^3}{\eta_1+h_1^3} \frac{\eta_1}{\eta_2}$. The effect of such a change on instability growth is however unclear and requires further simulation work. For PS molecular weights of 2.4 and 212 kg/mol, h_c corresponds to 13 nm [45] and 23 nm [46] respectively at a temperature of 440 K, and a similar scale of 10-20 nm is expected for PS100-PMMA100. Values of $h \sim 10$ nm additionally require the currently neglected inclusion of Van der Waal interactions in the model. Future work should therefore explore the dependence of mobility on film thickness and incorporate the Van der Waal interactions.

In a related study[47] on the long-wave Marangoni instability of heated thin polymer films, evidence for chain alignment was found, which is caused by the confinement and thermal conductivity of a thin polymer layer. As previously observed[48], such an alignment increases with

 This journal is © The Royal Society of Chemistry [year]

decreasing molecular weight and decreasing film thickness and might be able to induce changes in film mobility in very thin films. This implies the existence of a threshold thickness, below which a change in mobility (most probably due to a reduction in viscosity) would appear.

The increases in the thinner film mobility might also be due to higher stresses causing the polymer film to slip. The shear stress increases at larger instability amplitudes. If there is a critical stress where the polymer starts to slip, it would be exceeded in thinner films. Once a film starts to locally slip, the growth rate would accelerate, leading to a more rapid drop formation compared to a thicker film.This could erroneously be interpreted in terms of a reduction in film viscosity where, in fact, higher stresses act to increase polymer flow.

Finally, we discuss a further issue that has, to our knowledge, not yet been studied for two-layer configurations but might be of relevance for the observed topographies. In general, for one-layer thin films, one distinguishes dewetting via a spinodal surface instability and via homogeneous or heterogeneous nucleation (e.g.[8,14,49,50]). Most authors relate the respective processes to linearly unstable and metastable (i.e. linearly stable but unstable with respect to finite size perturbations) films, respectively. The situation is however more complex as even within the linearly unstable regime nucleation can under certain conditions dominate[15,50]. The distinction of the processes is difficult and requires a careful analysis of the evolving topographies. It has been shown that individual nucleated structures evolve in parallel with a spontaneous surface instability, resulting in nucleated holes with satellite holes or rims (depending on the stage of the evolution) in a background of a labyrinthine pattern[39].

Similar issues have not yet been studied for two- or multilayer systems where such effects might lead to intricate behaviour depending on the ratio of the amplitudes of the initial roughness of the films, and properties of additional finite size defects. Furthermore, one may speculate that a layer of larger mobility (and possibly larger initial roughness) evolves structures of large amplitude much faster then the other layer. The resulting large amplitude structures may then act as finite size defects for the other layer and effectively trigger an evolution via the nucleation pathway. Although, we have not seen such a behaviour in the simulations it might be possible to find it via an extensive parameter scan, involving, e.g. changes to the ratio of the initial roughness. This goes beyond the scope of the present work and should be further investigated in the future.

We acknowledge support by the EU [MRTN-CT-2004005728 (PATTERNS), PERG04-GA-2008-239426 (POLYPATT) and PITN-GA-2008-214919 (MULTIFLOW)], and SFI for NAP200.

A Linear analysis of general case

The main text presented analytical results for the linear phase of evolution for the special case when mobility ratio m and surface tension ratio σ are both equal to one. Here, we give further results that are valid in the general case where m and σ can differ from one. The Jacobian matrix reads

$$\mathbf{J}_k = -H_1^3 k^2 \begin{bmatrix} f_{11}+k^2 & f_{12} \\ m f_{12} & m(f_{22}+\sigma k^2) \end{bmatrix}$$

with

$$k_c^2 = -\operatorname{tr}(\mathbf{E}_0) = 2\left(\frac{1}{\epsilon_2}-1\right)^2 \frac{1+\sigma\alpha^2}{\sigma}$$

then

$$\begin{aligned} \operatorname{tr}(\mathbf{J}) &= -H_1^3 k^2 \left[(1+m\sigma)\,k^2 - \frac{m\sigma+\sigma\alpha^2}{1+\sigma\alpha^2} k_c^2\right], \\ \det(\mathbf{J}) &= m\sigma H_1^6 k^6 \left(k^2-k_c^2\right). \end{aligned}$$

The determinant vanishes for the two wavenumbers

$$\begin{aligned} k &= 0 \\ k &= k_c, \end{aligned}$$

where k_c is the critical wavenumber. This implies the system is unstable with respect to modes with wavenumbers within the unstable band from $k=0$ to $k-k_c$.

Defining

$$\triangle = \operatorname{tr}(\mathbf{J})^2 - 4\det(\mathbf{J}) \tag{17}$$

and

$$A = \frac{1}{2\sigma\alpha}\left[\left(\sigma\alpha^2+1\right)(1-m\sigma)\frac{k^2}{k_c^2} + m\sigma - \sigma\alpha^2\right] \tag{18}$$

and obtains the eigenvalues $\beta_\pm$ and the corresponding eigenvectors $\xi_\pm$ of the Jacobian $\mathbf{J}_k$

$$\beta_\pm = \frac{1}{2}\left(\operatorname{tr}(\mathbf{J}) \pm \sqrt{\triangle}\right) = \frac{H_1^3 k_c^4}{2} f_\pm(m,\sigma,\alpha,\frac{k}{k_c}) \tag{19}$$

$$\chi_\pm = A \pm \sqrt{A^2+m} = g_\pm(m,\sigma,\alpha,\frac{k}{k_c}), \tag{20}$$

respectively, where $f_\pm$ and $g_\pm$ are functions depending only on m,σ,α, and k/k_c. Note that χ_ϵ has the same sign as ϵ, i.e., there exists always one mirror mode and one zig-zag mode associated respectively to β_+ and β_-. To determine the sign of the growth rates, we consider the two cases where $k > k_c$ and $0 < k < k_c$.

- For $k > k_c$, then $\det(\mathbf{J}) > 0 \implies \triangle < \mathrm{tr}(\mathbf{J})^2$ and then $\beta_\pm$ has the sign of $\mathrm{tr}(\mathbf{J})$ which is negative: thus $\beta_\pm < 0$.

- For $k < k_c$, then $\det(\mathbf{J}) < 0$ the eigenvalues have opposite signs because $\triangle > \mathrm{tr}(\mathbf{J})^2$ then

$$\beta_+ > 0, \qquad \beta_- < 0.$$

Moreover, the sign of χ_+ is positive, and χ_- is negative. Therefore, in the generic case where m and σ are not necessarily equal to one, the zig-zag mode is stable and the mirror mode is unstable in the range $[0, k_c]$.

The roughness of film j is the standard deviation of the film height R_j. Assuming the Fourier mode at $k_{\max}$ is dominant, the roughness R_j follows

$$\begin{aligned} R_j^2 &= \frac{\int_0^{2\pi/k_{\max}} \left[\xi\chi_j \exp\left(\beta t + ik_{\max}x\right)\right]^2 \, \mathrm{d}x}{\int_0^{2\pi/k_{\max}} \mathrm{d}x} \\ R_j &= \frac{\xi}{\sqrt{2}}\chi_j \exp\left(\beta t\right) \\ \Rightarrow \frac{R_2}{R_1} &= \frac{\chi_2 \exp\left(\beta t\right)}{\chi_1 \exp\left(\beta t\right)} = \chi_{\max}. \end{aligned}$$

Thus the ratio of the roughnesses of the two films is then $\chi_{\max}$.

B Critical and fastest mode

The dimensional critical wavenumber is

$$k_c = \sqrt{2}\frac{\epsilon_0^{1/2}\epsilon_a^{1/2}\left|U\right|}{\sigma_2^{1/2}}\left(\sigma\alpha^2+1\right)^{1/2}\left(1-\frac{1}{\tilde{\epsilon}_2}\right)\left|\tilde{f}_{el}\right|^{3/2} \tag{21}$$

which does not depend on the viscosity. There is at least one maximal growth rate $\beta_{\max} = \beta_+(k_{max})$ where the value k_{max} $(0 < k_{\max} < k_c)$ is obtained by determining the maximum of the growth rate β_+, i.e. by solving

$$\frac{d\beta_+}{dk} = 0. \tag{22}$$

According to Eq. (19) and Eq. (20), the ratio $k_{\max}/k_c$ and the ratio of roughnesses $\frac{\chi_2 \exp(\beta t)}{\chi_1 \exp(\beta t)} = \chi_{\max}$ of the fastest growing mode $k_{\max}$ only depend on ratios of fluid properties, i.e. m, σ and α but not on U and d, i.e. the capacitor properties. Therefore, m, σ and α determine the linear regime. The other parameters, in particular the capacitor properties U and d, only scale space and time.

References

1 P.-G. de Gennes, *Rev. Mod. Phys.*, 1985, **57**, 827–863.
2 V. S. Mitlin, *J. Colloid Interface Sci.*, 1993, **156**, 491–497.
3 S. J. VanHook, M. F. Schatz, J. B. Swift, W. D. McCormick and H. L. Swinney, *J. Fluid Mech.*, 1997, **345**, 45–78.
4 U. Thiele and E. Knobloch, *Physica D*, 2004, **190**, 213–248.
5 R. Mukherjee, A. Sharma, G. Patil, D. Faruqui and P. S. G. Pattader, *Bull. Mat. Sci.*, 2008, **31**, 249–261.
6 E. Schäffer, T. Thurn-Albrecht, T. P. Russell and U. Steiner, *Europhys. Lett.*, 2001, **53**, 518–524.
7 Z. Lin, T. Kerle, S. M. Baker, D. A. Hoagland, E. Schäffer, U. Steiner and T. P. Russell, *J. Chem. Phys.*, 2001, **114**, 2377–2381.
8 G. Reiter, *Phys. Rev. Lett.*, 1992, **68**, 75–78.
9 R. Seemann, S. Herminghaus and K. Jacobs, *Phys. Rev. Lett.*, 2001, **86**, 5534–5537.
10 A. Oron, S. Davis and S. Bankoff, *Rev. Mod. Phys.*, 1997, **69**, 931–980.
11 R. V. Craster and O. K. Matar, *Rev. Mod. Phys.*, 2009, **81**, 1131–1198.
12 U. Thiele, in *Thin films of Soft Matter*, ed. S. Kalliadasis and U. Thiele, Springer, Wien, 2007, ch. Structure formation in thin liquid films, pp. 25–93.
13 U. Thiele, *J. Phys.-Cond. Mat.*, 2010, **22**, 084019.
14 J. Becker, G. Grün, R. Seemann, H. Mantz, K. Jacobs, K. R. Mecke and R. Blossey, *Nat. Mater.*, 2003, **2**, 59–63.
15 U. Thiele, M. G. Velarde and K. Neuffer, *Phys. Rev. Lett.*, 2001, **87**, 016104.
16 R. Blossey, *Phys. Chem. Chem. Phys.*, 2008, **10**, 5177–5183.
17 E. Schaffer, T. Thurn-Albrecht, T. Russell and U. Steiner, *NATURE*, 2000, **403**, 874–877.
18 N. Wu and W. B. Russel, *Nano Today*, 2009, **4**, 180–192.
19 D. R. Barbero and U. Steiner, *Phys. Rev. Lett.*, 2009, **102**, year.
20 P. Goldberg-Oppenheimer and U. Steiner, *Small*, 2010, **6**, 1248–1254.
21 D. Merkt, A. Pototsky, M. Bestehorn and U. Thiele, *Phys. Fluids*, 2005, **17**, 064104.
22 N. E. Voicu, S. Harkema and U. Steiner, *Advanced Functional Materials*, 2006, **16**, 926–934.
23 Z. Lin, T. Kerle, T. Russell, E. Schaffer and U. Steiner, *Macromolecules*, 2002, **35**, 3971–3976.
24 Z. Lin, T. Kerle, T. Russell, E. Schaffer and U. Steiner, *Macromolecules*, 2002, **35**, 6255–6262.
25 T. Russell, Z. Lin, E. Schaffer and U. Steiner, *Fibers and Polymers*, 2003, **4**, 1–7.
26 A. Pototsky, M. Bestehorn, D. Merkt and U. Thiele, *Europhys. Lett.*, 2006, **74**, 665–671.
27 A. Pototsky, M. Bestehorn, D. Merkt and U. Thiele, *J. Chem. Phys.*, 2005, **122**, year.
28 A. Pototsky, M. Bestehorn, D. Merkt and U. Thiele, *Phys. Rev. E*, 2004, **70**, year.
29 M. Morariu, N. Voicu, E. Schaffer, Z. Lin, T. Russell and U. Steiner, *Nat. Mat.*, 2003, **2**, 48–52.
30 K. Leach, S. Gupta, M. Dickey, C. Willson and T. Russell, *Chaos*, 2005, **15**, year.
31 M. D. Morariu, N. E. Voicu, E. Schäffer, Z. Lin, T. P. Russell and U. Steiner, *Nature Materials*, 2003, **2**, 48–52.
32 D. Bandyopadhyay, R. Gulabani and A. Sharma, *Ind. Eng. Chem. Res.*, 2005, **44**, 1259–1272.
33 D. Bandyopadhyay, A. Sharma, U. Thiele and P. D. S. Reddy, *Langmuir*, 2009, **25**, 9108–9118.

 This journal is © The Royal Society of Chemistry [year]

34 S. Srivastava, D. Bandyopadhyay and A. Sharma, *Langmuir*, 2010, **26**, 10943–10952.

35 D. W. van Krevelen, *Properties of Polymers: Their estimation and correlation with chemical structure*, Elsevier Scientific Publishing Company, Amsterdam-Oxford-New York, 1976.

36 J. Ferry, *Viscoelastic properties of polymers*, John Wiley & Sons, Inc., New York-Chichester-Brisbane-Toronto, 1980.

37 J. Mark, *Physical properties of polymer handbook*, American Institute of Physics, 1996.

38 R. A. Friesner, L. S. Tuckerman, B. C. Dornblaser and T. V. Russo, *Journal of Scientific Computing*, 1989, **4**, 327–354.

39 P. Beltrame and U. Thiele, *S. J. App. Dyn. Sys.*, 2010, **9**, 484–518.

40 P. Beltrame, E. Knobloch, P. Hänggi and U. Thiele, *Phys. Rev. E*, 2011, **83**, 016305.

41 P. Goldberg-Oppenheimer and U. Steiner, *Small*, 2010, **6**, 1248–1254.

42 G. Amarandei, *Electronic supplementary material at [URL to be inserted]*, 2012.

43 N. E. Voicu, S. Ludwigs and U. Steiner, *Advanced Materials*, 2008, **20**, 3022–3027.

44 T. Koga, C. Li, M. K. Endoh, J. Koo, M. Rafailovich, S. Narayanan, D. R. Lee, L. B. Lurio and S. K. Sinha, *Phys. Rev. Lett*, 2010, **104**, year.

45 Z. Yang, Y. Fujii, F. K. Lee, C.-H. Lam and O. K. C. Tsui, *Science*, 2010, **328**, 1676–1679.

46 Z. Yang, A. Clough, C.-H. Lam and O. K. C. Tsui, *Macromolecules*, 2011, **44**, 8294–8300.

47 E. McLeod, Y. Liu and S. M. Troian, *Phys. Rev. Lett.*, 2011, **106**, 175501.

48 Y. Cohen and S. Reich, *J. Poly. Sci. B*, 1981, **19**, 599–608.

49 R. Seemann, S. Herminghaus and K. Jacobs, *J. Phys.: Condens. Matter*, 2001, **13**, 4925–4938.

50 U. Thiele, *Eur. Phys. J. E*, 2003, **12**, 409–416.

Supplementary materials for:
Pattern formation induced by an electric field in a polymer-air-polymer thin film system
Soft Matter, DOI:10.1039/b000000x
G. Amarandei, P. Beltrame, I. Clancy, C. O'Dwyer, A. Arshak, U. Steiner, D. Corcoran and U. Thiele

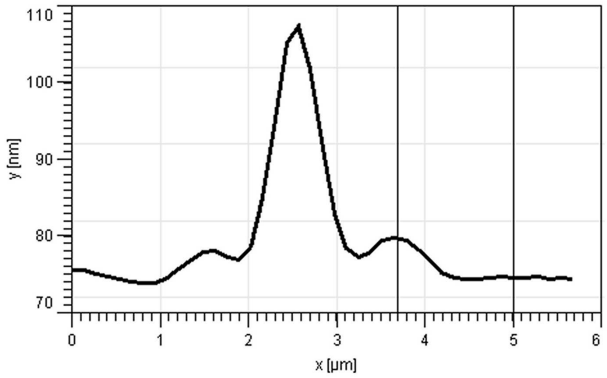
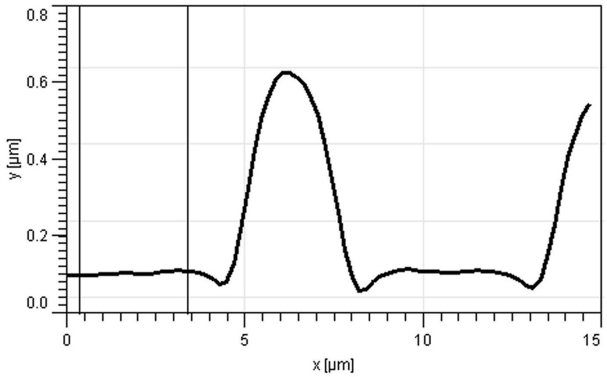
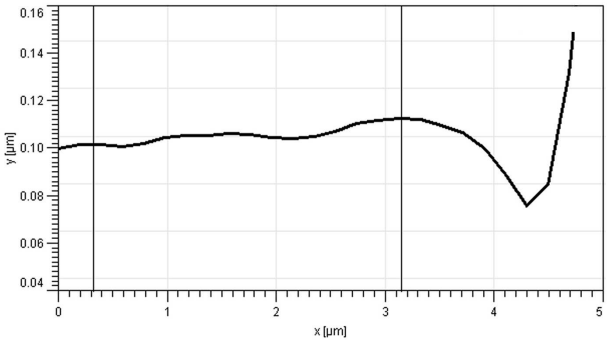


Fig. S1: (a) Cross section of a PS100 drop structure with two symmetric satellites from the PS10-PS100 experiment. The satellite height is measured from the flat film surface.



(a)



(b)

Fig. S 2: (a) Cross section of the drop structures in PMMA100 from the PS100-PMMA100 experiment and (b) a zoom in on this profile emphasizing the rim present around one of the features. The rim height is measured from the flat film surface.

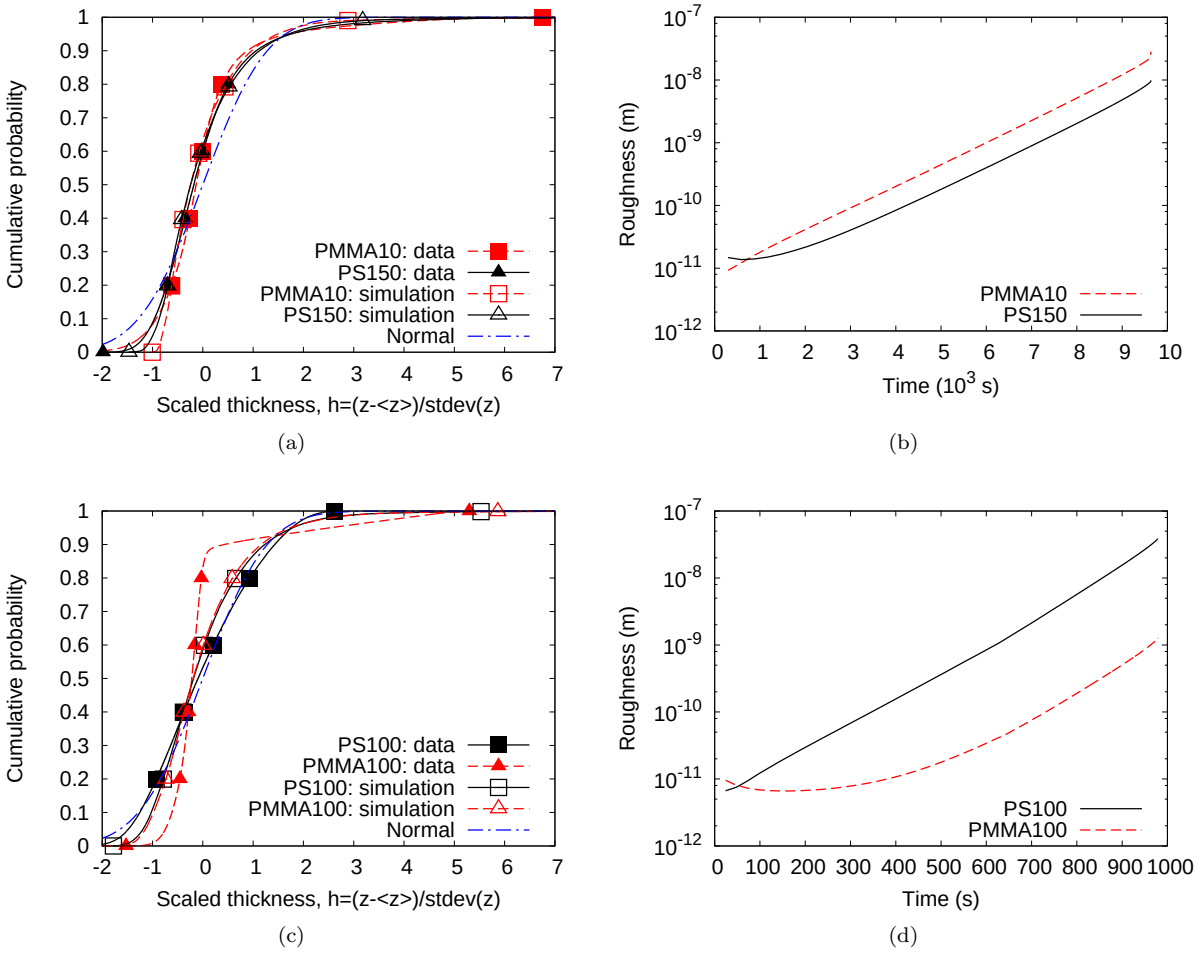


Fig. S3: The cumulative distributions of the film thicknesses for experiment and simulation in (a) PMMA10-PS150, and (c) PS100-PMMA100 systems. The cumulative distributions have been normalized such that their mean is zero and their standard deviation allows one to directly compare the forms of the distributions. The time dependence of the roughness of each film as predicted by the 3d model is presented in (b) for PMMA10-PS150, and (d) for PS100-PMMA100 systems.